HHS Public Access

Author manuscript

Anal Bioanal Chem. Author manuscript; available in PMC 2020 August 01.

Published in final edited form as:

Anal Bioanal Chem. 2019 August ; 411(21): 5405–5413. doi:10.1007/s00216-018-1440-9.

3D Printed Microfluidic Devices with Immunoaffinity Monoliths for Extraction of Preterm Birth Biomarkers

Ellen K. Parker[†], **Anna V. Nielsen**[†], **Michael J. Beauchamp**[†], **Haifa M. Almughamsi**[†], **Jacob B. Nielsen**[†], **Mukul Sonker**[†], **Hua Gong**[‡], **Gregory P. Nordin**[‡], **Adam T. Woolley**[†,*]

[†]Department of Chemistry and Biochemistry, C100 BNSN, Brigham Young University, Provo, UT 84602, USA

[‡]Department of Electrical and Computer Engineering, Brigham Young University, 459 CB, Brigham Young University Provo, UT 84602, USA

Abstract

Preterm birth (PTB) is defined as birth before the 37th week of pregnancy and results in 15 million early deliveries worldwide every year. Presently, there is no clinical test to determine PTB risk; however, a panel of nine biomarkers found in maternal blood serum has predictive power for a subsequent PTB. A significant step in creating a clinical diagnostic for PTB is designing an automated method to extract and purify these biomarkers from blood serum. Here, microfluidic devices with 45 μm × 50 μm cross-section channels were 3D printed with a built-in polymerization window to allow a glycidyl methacrylate monolith to be site-specifically polymerized within the channel. This monolith was then used as a solid support to attach antibodies for PTB biomarker extraction. Using these functionalized monoliths, it was possible to selectively extract a PTB biomarker, ferritin, from buffer and a human blood serum matrix. This is the first demonstration of monolith formation in a 3D printed microfluidic device for immunoaffinity extraction. Notably, this work is a crucial first step toward developing a 3D printed microfluidic clinical diagnostic for PTB risk.

Keywords

3D printing; integrated microfluidics; monoliths; point-of-care; sample preparation; sample purification

1 Introduction

Preterm birth (PTB) is defined by the World Health Organization as birth before the 37th week of pregnancy [1]. Over 15 million babies, or 1 in 10, are born preterm each year worldwide [2], and one million of those babies die every year due to complications of PTB.

[*]Corresponding author, atw@byu.edu.

Conflicts of Interest

The authors declare no conflicts of interest for this work.

Research Involving Human Participants

Human blood serum samples were obtained from commercial sources; human subjects work has been approved under IRB# E18401.

The survivors face several health and developmental problems including cerebral palsy, chronic lung disease, vision or hearing loss, and intellectual impairment [3–4]. If PTB imminence is suspected, shots, often containing progesterone, can be administered to prevent or delay delivery [5]. However, PTB risk is often unknown until early labor has already begun. If a clinical test existed to predict PTB risk well before contractions took place [3], more could be observed and understood about underlying causes of and preventative measures for PTB. Esplin et al. [6] evaluated nine biomarkers that have 87% selectivity and 81% specificity for predicting a subsequent PTB. We are working to make a clinical and potentially point-of-care test (POCT) based on these biomarkers to predict PTB risk [7–9].

An important aspect of POCTs is the need for simple and effective sample preparation, often from complex biological matrices [10–11]. Monoliths, continuous porous polymers used as stationary phases in liquid chromatography [12–13], are one such sample preparation tool. Monoliths have advantages over traditional packed columns because they offer higher flow rates, lower backpressure, and reduced mass transfer resistance [14–15]. Similar to packed beads, monoliths can also be functionalized [16], for example, by chemically modifying unreacted functional groups present in the monolith such as epoxy, hydroxyl, or aldehyde groups, or by incorporating prefunctionalized monomers into the monolith mixture prior to polymerization [17]. These functionalities allow monoliths to be used for a variety of applications including cation and anion exchange, metal ion affinity, and protein affinity separations [18]. For example, we previously demonstrated the ability to form immunoaffinity monoliths [19–20] and have extracted PTB biomarkers from a human blood serum matrix in conventionally fabricated microfluidic devices [8]. Finally, monoliths can be fabricated *in situ* [21] by polymerizing a mixture of monomers, porogens, and a free radical initiator. For these reasons, monoliths are often used in microfluidic applications [13,22].

Microfluidic POCTs offers many advantages for designing fluid-based assays including smaller liquid volume requirements, less waste generated [10,23], portability [24], and integration of many sample preparation and detection processes on the same chip [25–26]. However, a persistent limitation of microfluidics is the challenge of fabricating complex integrated designs with detailed 3D structures. For simple designs such as a traditional “T-shape”, fabrication has become automated and commercialized through injection molding or machining. Unfortunately, more complex layouts with multiple channels, pumps and valves, or other 3D features require special equipment and trained personnel to ensure that all the layers are designed, fabricated, and aligned correctly [22]. Additionally, conventional planar micromachining is resource intensive, requiring a cleanroom environment and safety apparatus for corrosive or toxic chemicals. Thus, many researchers have looked to 3D printing as a means of overcoming this limitation for fabricating complex fluidic layouts.

3D printing is a layer-by-layer additive manufacturing technique [27] that is becoming a common tool for rapid prototyping in jewelry making, dentistry, and auto manufacturing [28–29], as well as in fluidic applications [30–34]. 3D printing offers several advantages over traditional microfabrication techniques for making complex fluidic devices including: significantly faster fabrication times [35], cheaper and/or less equipment and chemicals [25], easier use, and the ability to take full spatial advantage of three-dimensional manufacturing

[35]. 3D printing also provides the ability to easily make complex fluidic networks by removing time consuming and error prone alignment and bonding steps, which are currently not amenable to large-scale manufacturing with conventional fabrication techniques such as embossing or injection molding. Additionally, reengineering a 3D print design has a much quicker turnaround time compared to conventional methods. However, commercial 3D printing methods are not able to rapidly form truly microfluidic (<100 μm cross-section) features that are needed for many high-performance assays. One type of 3D printing, stereolithography, uses a vat of liquid resin which is photopolymerized, typically using UV LED light patterned by a projector or a scanned laser. Stereolithographic 3D printing is advantageous because unpolymerized resin can be more easily flushed from void spaces to create fluidic features, compared to other 3D printing techniques [36–38]. Furthermore, the printing resin composition can be customized for the application as long as it is photopolymerizable by the printer light source [39].

In this paper, we use a custom stereolithographic 3D printer and resin previously designed for making truly microfluidic features [40]. We 3D printed 45 μm × 50 μm enclosed microfluidic channels for immunoaffinity extraction of PTB biomarkers on a porous polymer monolith. A monolith polymerization window in the device design takes advantage of the inherent resin UV absorption properties for spatially selective and reproducible polymerization of a monolith within the microfluidic channels, the first demonstration of monolith formation in a 3D printed microfluidic device. After modifying these monoliths with antiferritin, qualitative extraction was demonstrated for ferritin, a PTB biomarker, using vacuum-driven flow. Additionally, we show extraction of ferritin from a human blood serum matrix. This is the first immunoaffinity extraction study to be performed in 3D printed microfluidic devices, demonstrating their excellent potential for use in future biological assays.

2 MATERIALS AND METHODS

2.1 Material sources

Tris hydrochloride, 3-(trimethoxysilyl)propyl methacrylate, dimethyl sulfoxide (DMSO), antiferritin, glycidyl methacrylate (GMA), ethylene glycol dimethacrylate (EDMA), 1-dodecanol, 2,2-dimethoxy-2-phenylacetophenone (DMPA), and polyethylene glycol)diacrylate (PEGDA, MW 250) were purchased from Sigma (St. Louis, MO). Sodium phosphate, sodium bicarbonate, sodium carbonate, boric acid, ferritin and Amicon ultra 0.5 mL centrifugal filters (3, 10, or 30 kDa cutoff) were purchased from Millipore Sigma (Burlington, MA). All solutions were made using deionized water (18.3 MΩ·cm) filtered by a Barnstead EASYpure UV/UF system (Dubuque, IA). Toluene and 2-propanol (IPA) were from Macron (Center Valley, PA). Acetone, Tris base, and Alexa Fluor 532 (carboxylic acid, succinimidyl ester) were obtained from Fisher Scientific (Fair Lawn, NJ). Sodium hydroxide and Tween 20 were purchased from Mallinckrodt Baker (Paris, KY). Glass slides for 3D printing were purchased from VWR (Radnor, PA). Cyclohexanol came from Spectrum (New Brunswick, NJ). 2-nitrophenyl phenyl sulfide (NPS) was purchased from TCI (Portland, OR). Dry milk was obtained from Walmart (Bentonville, AR). Corticotropin releasing factor was from GeneScript (Piscataway, NJ). Female human blood serum (off-the-clot, sterile

filtered) was purchased from Zen-Bio (Research Triangle Park, NC). Phenylbis(2,4,6-trimethylbenzoyl)phosphine oxide (Irgacure 819) was provided by BASF (Mississauga, ON).

2.2 3D Printing of Devices

A custom stereolithographic 3D printer created microfluidic devices as described previously [40]. Briefly, this printer uses a 385 nm LED and has a pixel size of 7.6 μm in the image plane with 21.2 $mW \cdot cm^{-2}$ irradiance. The build area of the printer is 19 mm × 12 mm. The build layer height is 10 μm and the normal exposure time is 700 ms per layer. The first four layers of the print are overexposed for 20, 10, 5 and 1 s to ensure device attachment to the glass slide. After the microfluidic devices are printed, excess resin is washed out with IPA, and the channels are vacuumed dry. Then, the devices are placed under an 11 mW, 430 nm LED (ThorLabs, Newton, NJ) for ~20 min for post curing. Post curing is done at a longer wavelength than device printing, because at 430 nm the UV absorber (NPS) no longer absorbs light but the photoinitiator (Irgacure 819) is still effective.

Glass microscope slides (3 in × 1 in × 1 mm) were prepared for 3D printing by scoring the slides into thirds using a laser cutter (Universal Laser Systems, Scottsdale, AZ). The settings on the laser cutter were 50% power, 10% speed, and 165 pulses per inch. The glass slides were then cleaned with acetone and IPA and dried. The glass treatment solution was prepared by making a 10% (v/v) solution of 3-(trimethoxysilyl)propyl methacrylate in toluene. The glass slides were functionalized in this solution for 2 h, after which they were taken out, washed with IPA, and dried. The glass slides were sectioned to the appropriate size for the 3D printer along the scored marks, and then stored in toluene until use.

The 3D printing resin was prepared by making a solution of 2% NPS and 1% Irgacure 819 in 97% PEGDA [40]. The solution was sonicated until all components were dissolved and then stored in an amber bottle wrapped in foil to prevent premature polymerization.

The 3D print was designed using the open source CAD software OpenSCAD (openscad.org), as shown in Figure 1A. The 3D print is 1.6 mm tall, 12 mm long, and 19 mm wide. The design contains three divisions that result in four discrete modules. Each module has a straight channel that is 5 layers (50 μm) tall by 6 pixels (45 μm) wide by 4.9 mm long, with 2.7 mm diameter reservoirs on each end. A 600 μm wide monolith polymerization window (MPW) is six layers above the top of the channel and spans the width of each module. We initially tested a different device design that had 9 channels, smaller reservoirs, and no module divisions, as shown in the Electronic Supplementary Material (ESM), Fig. S1.

A channel edge exposure technique described previously [40,41] ensured that the channels were printed with their designed width. Briefly, this technique uses two different exposures in a given layer for areas surrounding the channel. First, a 400 ms exposure occurs everywhere except for the 3 pixels adjacent to either side of the channel, the 4 layers above the channel, and in the channel itself. Then a 330 ms exposure is done everywhere except in the channel itself. These dual exposures per layer near the channels help them to remain open by lessening light scattering and undesired light penetration in the channels.

2.3 Monolith Preparation

Two different GMA-EDMA monolith recipes were tested. Monolith 1 was prepared using 20% GMA, 10% EDMA, 25% cyclohexanol, 25% 1-dodecanol, and 20% Tween 20 [8]. Monolith 2 was prepared using 24% GMA, 11% EDMA, 10% cyclohexanol and 55% 1-dodecanol. Both mixtures were sonicated for 10 min, DMPA was added to make the solution 1% DMPA by mass, and the mixtures were sonicated for an additional 10 min. Prepolymer solution was loaded into one or more channels and the device was then placed under a SunRay 600 UV lamp (Uvitron, West Springfield, MA) for 10 min of UV exposure. The unpolymerized resin was then removed from the monolith by flushing the channel with IPA for 30 min. The monolith was emptied using vacuum and stored dry until use.

Monoliths were characterized by scanning electron microscopy (SEM) imaging. Specimens were prepared by removing 3D printed devices from the glass slide and cutting through the MPW using a razor blade. The pieces were then sputter coated with 80:20 Au:Pd, and images were taken using an ESEM XL30 (FEI, Thermo Fisher, Fair Lawn, NJ) in high vacuum mode at 10 kV electron beam potential. The nodule and pore sizes were analyzed from the SEM images using ImageJ (NUT, Bethesda, MD).

2.4 Antibody Characterization and Immobilization

The compatibility of our antiferritin and ferritin samples was evaluated using a dot blot test. Ferritin (2 μL of a 1 μg/mL solution in 20 mM phosphate buffer pH 7) was dotted on nitrocellulose paper (Bio-Rad, Hercules, CA). The remaining exposed part of the nitrocellulose paper was blocked for 1 h with a solution of 5% dry milk in a 50 mM Tris, 0.5 M NaCl, and 0.05% Tween 20 buffer (TBST, pH 7.4). After blocking, the nitrocellulose paper was washed three times with TBST for 5 min. The paper was then incubated in antiferritin (1 μg/mL in TBST) for 1 h. After incubation, the paper was rinsed three times with TBST for 5 min. Finally, the paper was incubated for 1 h with a secondary fluorescent antibody, IRDye 800CW goat anti-rabbit IgG (H+L) (Li-Cor, Lincoln, NE), at a concentration of 1 μg/mL in TBST. Afterward, the paper was washed twice with TBST for 5 min followed by a 10 min rinse with Tris buffer-saline (TBS). The papers were then imaged on a Li-Cor Odyssey CLx scanner.

To immobilize antibody on the monolith, 5 μL of antibody solution (2 mg/mL in borate buffer pH 8.5) was added to one of the reservoirs and allowed to flow through the channel by capillary action. After the entire channel was filled, both reservoirs were emptied and then refilled with 20 mM borate buffer, pH 8.5, and the antibody solution was left to immobilize overnight. Next, the channel was filled with 0.1 M Tris buffer, pH 8.5, and left for 1 h to block any remaining reactive sites on the monolith. Finally, the monoliths were washed with 20 mM phosphate buffer pH 7 to remove the excess Tris buffer. For control experiments, no antibody was added but the monolith was still blocked with Tris buffer.

2.5 Sample Preparation

Ferritin and antiferritin were fluorescently labeled by dissolving in 10 mM bicarbonate buffer (BCB, pH 10), and adding Alexa Fluor 532 dissolved in DMSO. Labeling was performed at a dye:ferritin molar ratio of 30:1 and a dye:antibody molar ratio of 10:1. The

solutions were incubated overnight in the dark at room temperature. Afterward, the solutions were filtered four times for 15 min at 14000 RPM using a 30 or 10 kDa filter, respectively, to remove excess dye. Working solutions of the labeled ferritin were prepared in 20 mM phosphate, pH 7, and the antibodies were prepared in 20 mM borate buffer pH 8.5. CRF was labeled in a similar fashion with a dye:biomarker ratio of 3:2 and filtered with a 3 kDa filter.

A spiked sample was made by adding labeled ferritin to yield a 50 nM concentration in human blood serum (5-fold diluted in 20 mM phosphate buffer, pH 7). Known PTB biomarker risk levels range from mid-picomolar to low micromolar [6, 9], so the 50 nM ferritin concentration is reasonable for initial testing. Microchip electrophoresis was carried out on both the ferritin and spiked serum samples to confirm labeling (data not shown).

2.6 Experimental Setup

A laser induced fluorescence (LIF) detection system used a 532 nm laser (Laserglow Technologies, Toronto, ON) directed into a Zeiss Axio Oberserver.A1 inverted microscope (Jena, Germany) with a Chroma ET-532 nm laser bandpass filter set (Rockingham, VT). Images were taken using a Photometrics coolSNAP HQ2 CCD camera (Tucson, AZ) and a 4× microscope objective. CCD images were taken with exposure times between 100–400 ms and analyzed using ImageJ. Platinum electrodes were used to apply the desired voltages to the channels from a high voltage power supply (Stanford Research Systems, Sunnyvale, CA).

For experiments, the channels were first filled with 20 mM phosphate buffer, pH 7, and vacuum was applied to the reservoir further from the monolith for 1 min to equilibrate the channel. Next, the reservoirs were emptied; labeled sample was added to the reservoir nearer to the monolith, and the other reservoir was refilled with fresh phosphate buffer. Vacuum was applied for 1 min to load the sample through the channel. After vacuum was removed, the PTB analyte was allowed to incubate for 10 min with the antibody on the monolith. Then, both reservoirs were washed three times and filled with phosphate buffer, and vacuum was reapplied for 5 min for rinsing. This process was repeated twice until the entire channel was rinsed out (except for any analyte bound to the antibody on the monolith). Rinse efficiency was confirmed by CCD imaging of the monolith. Finally, the rinsing buffer was removed from both reservoirs, elution buffer (50 mM BCB pH 10) was added, and vacuum was reapplied for 2 minutes.

3 RESULTS AND DISCUSSION

3.1 3D Printed Device Printing Parameters and Features

The first step to developing a 3D printed microfluidic device for immunoaffinity extraction of PTB biomarkers was to make a design containing all of the necessary features for immunoaffinity extraction: reservoirs, channels, and a monolith. An initial design contained nine such features (ESM, Fig. S1) with 45 μm wide × 50 μm tall × 4.3 mm long channels with 1.8 mm diameter reservoirs (~4 μL volume). Although this design offered high channel density, it also had flaws. First, the tall, narrow reservoirs made liquids in the channels prone to gravity-induced flow with only small differences in fluid level, for example due to

evaporation. Secondly, cracking was sometimes observed between channels (ESM, Fig. S2), making it difficult to get consistent results.

An improved device was thus designed (Fig. 1), which contained four identical channels in discrete modules, each separated by a 0.5 mm gap. This gap provided an assurance against fluid leakage between channels, and the smaller modules had less stress than in larger polymerized devices. Furthermore, the reservoirs were resized to have a 2.7 mm diameter (~6 μL volume), reducing channel length to 22 mm. The device height was decreased to 1.2 mm to reduce gravity-induced flows; this shorter device height also reduced material stress and improved stability toward cracking. Optimizing the layer exposure and channel compensation times should also help to reduce material stress.

The final important feature of note in both the initial and improved device designs is a monolith polymerization window, a trench that runs perpendicular to the channels and allows for polymerization of the monolith. The MPW is necessary because the 3D printing resin contains a UV absorber, which does not allow for sufficient penetration of UV light necessary to polymerize monoliths. By creating a trench whose bottom is six layers (60 μm) above the channel top, the material above the channel was thin enough to allow UV light through to polymerize the monolith in this region. In this way, the MPW utilized the inherent UV absorption properties of the resin to give precise and reproducible spatial selectivity over monolith formation. For these experiments, the MPW width (and thus the monolith length) was designed to be 600 μm, but it would be straightforward to design other lengths.

To show the precision and spatial selectivity afforded by the MPW in monolith formation, monoliths were polymerized in 3D printed devices using either a MPW or a chrome-glass mask. In both cases, the monolith was designed to be 600 μm long and was placed 1.2 mm from a reservoir. With the mask, monoliths were formed with a length of 607 ± 25 μm and a spatial precision of ± 65 μm (n = 8). Using the MPW, monoliths were 567 ± 14 μm long with a spatial precision of ± 17 μm (n = 8). Spatial precision for the MPW is limited by the monolith length, rather than variations in the MPW location in the 3D print. These results indicate that the MPW yields better monolith length precision, and considerably improved spatial positioning precision over monolith formation by an external mask. Additionally, the MPW is easier to place than an external mask since the alignment is integrated into the design. The MPW is most effective if the 3D printed material enclosing the channel is sufficiently thick (−500 μm) to mask the rest of the channel from unwanted polymerization (see ESM, Fig. S3).

3.2 Monolith Formulation and Modification

Previously, we developed an affinity monolith in conventionally fabricated microfluidic devices [8]. However, this monolith formulation utilized Tween 20, a surfactant, to aid with component solubility, but which was not essential for monolith formation. Additionally, Tween 20 can affect the surface of the created monolith. To simplify the monolith composition and to provide a more uniform surface, a new monolith formulation was developed that did not contain Tween 20 (see Section 2.3).

To compare the properties of both monolith formulations, several SEM images were taken of both types of monolith as seen in Figure 2. Panels A and C show the monolith formed in the microfluidic channels with good side attachment, while panels B and D give a zoomed view of the monoliths, allowing closer inspection of pore and nodule sizes. A comparison of the pore and nodule sizes showed that both were similar across the two formulations. The pore size for monolith 1 was 1.6 ± 1.1 μm (n = 40) and the nodule size was 2.5 ± 1.0 (n = 30); for monolith 2 the pore and nodule sizes were 2.4 ± 1.4 μm (n = 36) and 2.4 ± 1.0 μm (n = 38), respectively. Figures 2 A,C show that both monoliths have good attachment to the channel walls. A comparison of Figures 2B,D shows rougher nodules for monolith 2, but both monoliths had acceptable morphologies. These results confirm that monoliths can readily be formed in 3D printed microchannels.

To further characterize these monoliths, fluorescently labeled antiferritin was attached to monoliths made from both formulations. Attachment of the antibody was verified by CCD imaging before and after immobilization (Fig. 3A-B). Figure 3C shows that monolith 2 (without Tween 20) had nearly tenfold greater antibody attachment than monolith 1 (with Tween 20); this much greater antibody attachment is a favorable feature of monolith 2 for the capture of ferritin. Although the surface area of the two monoliths was not measured, we believe that the increased signal is either a result of greater surface area or surface reactivity for binding antiferritin.

3.3 Immunoaffinity Extraction of Ferritin

With the improved device design and using vacuum driven fluid flow, ferritin was extracted on and eluted from monoliths with or without immobilized antiferritin. First, ferritin/antiferritin specificity was confirmed using a dot blot test (ESM, Fig. S4). CCD images of the fluorescence on the monolith were taken after the loading, rinsing, and elution steps; and background-subtracted fluorescence on the monolith was calculated from the images. In these experiments we expect high signal during the loading step due to the presence of fluorescent material in the channel. For both control and test monoliths the signal should drop following the rinse steps, but the decrease should be much more pronounced on control monoliths. Test monoliths have antiferritin, which should retain the fluorescently labeled ferritin, such that during the elution step the signal from control monoliths should change little, but the signal from test monoliths should drop due to elution of bound ferritin.

Figure 4A shows that for the control monolith (lacking antiferritin), the signal dropped the most between the loading and rinse steps, and was more similar between the rinses and elution. This was the expected result, because the majority of the labeled ferritin should rinse out from the control monolith since there is no antibody to retain the ferritin. The residual signal after rinsing and elution is likely from nonspecifically adsorbed ferritin bound to the monolith. In contrast, when antiferritin is attached to the monolith, there is a smaller decrease in fluorescent signal between loading and rinsing than in the control, because ferritin retained by the antibody on the monolith does not wash off during the rinsing step. In these experiments a much larger, ~2 fold drop in fluorescence occurs between the rinse and the elution, indicating that much of the extracted ferritin was eluted. The signal in these experiments does not return to background levels after elution for control or test monoliths,

indicating incomplete recovery (~50%) of extracted sample. Recovery could be increased by lowering nonspecific adsorption through monolith formulation optimization. We note that there is little nonspecific adsorption on the 3D-printed device material, but that it primarily occurs on monoliths.

To test the selectivity of these antiferritin monoliths for ferritin, another PTB biomarker, CRF, was flowed through a monolith with attached antiferritin using the same conditions as for ferritin extraction except the CRF concentration was 20 fold higher. As seen in Figure 4B, the fluorescence signal from labeled CRF dropped significantly between the loading and rinse steps, indicating that CRF was not retained on the monolith. This drop in fluorescence was observed for monoliths with or without antiferritin, confirming the lack of retention of an off-target analyte.

In order to create a PTB risk analysis POCT, it must be possible to extract PTB biomarkers from a blood serum matrix. To evaluate the viability of our system for such a test, a human blood serum sample was spiked with ferritin and flowed through monoliths with or without antiferritin attached as shown in Figure 4C. The data show that the largest signal drop for the control is between the load and rinse steps, a statistically significant 57% decrease ($t = 11.5$, $p = 0.99$). In contrast, when antiferritin is attached to the monolith, the drop in signal between the load and rinse steps is not statistically significant at only 4.4%, ($t = 0.10$, $p = 0.99$). The largest drop in signal when antiferritin is attached to the monolith occurs between the rinse and elution steps, a statistically significant 33% decrease ($t = 1.92$, $p = 0.85$), while the difference between the rinse and the elution steps for the control at only 6% was not statistically significant ($t = 0.82$, $p = 0.85$). There is residual signal in both experiments, likely from nonspecific adsorption to the monolith as indicated earlier. The clear differences in column fluorescence between the experiments with or without attached antiferritin give strong support to the assertion that this PTB biomarker can be extracted from a serum sample using a 3D printed microfluidic device.

4 Conclusions

3D printing is a promising new method for the fabrication of microfluidic devices because it is quick, inexpensive, and convenient for making small, 3D features. Furthermore, 3D printing allows for iterative and symbiotic design, immediate fabrication, and testing. Here, we have shown that a 3D printed device for immunoaffinity extraction can be fabricated and improved to address issues found during experimentation. We also have demonstrated that through use of a custom resin formulation and printer, monoliths can be polymerized in a spatially selective manner through design of the 3D print and the inherent masking of the resin. Furthermore, we have shown qualitatively that a preterm birth biomarker, ferritin, can be extracted selectively with antiferritin in these 3D printed devices from both buffer and human blood serum matrices using vacuum driven flow. This is the first demonstration of a monolith-based extraction in a 3D printed microfluidic device.

A key contribution of this work is showing that extraction of a PTB biomarker from serum in 3D printed microfluidic devices is possible, an important step toward creating an integrated diagnostic. However, in order for this extraction to be combined with the other

parts of a PTB risk test, the process would need to be more automated, for example, by using on-chip pumps and valves [7,42–44]. This would allow for consistent flow rates and direct signal detection from eluted analytes. The final device will also incorporate on-chip concentration and labeling to improve detection limits. We further intend to make our method quantitative by detecting laser-induced fluorescence with a photomultiplier tube to enable limits of detection to be determined. Additional work will also be needed to decrease nonspecific adsorption on monoliths and to attach antibodies to multiple PTB biomarkers on monoliths. Importantly, as 3D printed microfluidic devices for immunoaffinity extraction are further developed and improved, more applications in bioanalysis should be realized.

Supplementary Material

Refer to Web version on PubMed Central for supplementary material.

Acknowledgments

The authors acknowledge support from the National Institutes of Health (R01 EB006124 and R15 GM123405-01A1). A.V.N. and M.J.B. thank the BYU Department of Chemistry and Biochemistry for financial support from a Roland K. Robins Fellowship, and H.M.A acknowledges Taif University for financial support.

References

1. World Health Organization. Preterm birth. In: Fact Sheets. WHO. 2018 http://www.who.int/mediacentre/factsheets/fs363/en/. Accessed 3 Jul 2018.
2. Centers for Disease Control and Prevention. Preterm birth. In: Maternal and Infant Health. CDC. 2018 https://www.cdc.gov/reproductivehealth/maternalinfanthealth/pretermbirth.htm. Accessed 3 Jul 2018.
3. Behrman RE, Butler AS. Preterm birth: causes, consequences, and prevention. Washington DC: National Academies Press; 2007.
4. Blencowe H, Cousens S, Oestergaard MZ, Chou D, Moller AB, Narwal R, Adler A, Garcia CV, Rohde S, Say L, Lawn JE. National, regional, and worldwide estimates of preterm birth rates in the year 2010 with time trends since 1990 for selected countries: a systematic analysis and implications. Lancet. 2012;379:2162–72. [PubMed: 22682464]
5. Roberto R, Sudhansu KD, Susan JF. Preterm labor: One syndrome, many causes. Science. 2014;345:760–5. [PubMed: 25124429]
6. Esplin MS, Merrell K, Goldenberg R, Lai Y, Iams JD, Mercer B, Spong CY, Miodovnik M, Simhan HN, van Dorsten P, Dombrowski M. Proteomic identification of serum peptides predicting subsequent spontaneous preterm birth. Am J Obstet Gynecol. 2011;204:391.e8. [PubMed: 21074133]
7. Sahore V, Sonker M, Nielsen AV, Knob R, Kumar S, Woolley AT. Automated microfluidic devices integrating solid-phase extraction, fluorescent labeling, and microchip electrophoresis for preterm birth biomarker analysis. Anal Bioanal Chem. 2018;410:933–41. [PubMed: 28799040]
8. Sonker M, Parker EK, Nielsen AV, Sahore V, Woolley AT. Electrokinetically operated microfluidic devices for integrated immunoaffinity monolith extraction and electrophoretic separation of preterm birth biomarkers. Analyst. 2018;143:224–31.
9. Nielsen AV, Nielsen JB, Sonker M, Knob R, Sahore V, Woolley AT. Microchip electrophoresis separation of a panel of preterm birth biomarkers. Electrophoresis. 2018;39:2300–7. [PubMed: 29683528]
10. Chin CD, Linder V, Sia SK. Commercialization of microfluidic point-of-care diagnostic devices. Lab Chip. 2012;13:2118–34.

11. Sonker M, Sahore V, Woolley AT. Recent advances in microfluidic sample preparation and separation techniques for molecular biomarker analysis: a critical review. Anal Chim Acta. 2017;986:1–11. [PubMed: 28870312]
12. Núñez O, Nakanishi K, Tanaka N. Preparation of monolithic silica columns for high-performance liquid chromatography. J Chromatogr A. 2008;1191:231–52. [PubMed: 18313061]
13. Knob R, Sahore V, Sonker M, Woolley AT. Advances in monoliths and related porous materials for microfluidics. Biomicrofluidics. 2016;10:032901–19. [PubMed: 27190564]
14. Andjelković U, Tufegdžić S, Popović M. Use of monolithic supports for high-throughput protein and peptide separation in proteomics. Electrophoresis. 2017;38:2851–69. [PubMed: 28906564]
15. Svec F, Lv Y. Advances and recent trends in the field of monolithic columns for chromatography. Anal Chem. 2015;87:250–73. [PubMed: 25375665]
16. Tetala KKR, Vijayalakshmi MA. A review on recent developments for biomolecule separation at analytical scale using microfluidic devices. Anal Chim Acta. 2016;906:7–21. [PubMed: 26772122]
17. Buchmeiser MR. Polymeric monolithic materials: syntheses, properties, functionalization and applications. Polymer. 2007;48:2187–98.
18. Masini JC, Svec F. Porous monoliths for on-line sample preparation: A review. Anal Chim Acta. 2017;964:24–44. [PubMed: 28351637]
19. Yang W, Sun X, Wang HY, Woolley AT. Integrated microfluidic device for serum biomarker quantitation using standard addition or a calibration curve. Anal Chem. 2009; 81: 8230–5 [PubMed: 19728735]
20. Yang W, Yu M, Sun X, Woolley AT. Microdevices integrating affinity columns and capillary electrophoresis for multibiomarker analysis in human serum. Lab Chip. 2010; 10: 2527–33. [PubMed: 20664867]
21. Svec F Porous polymer monoliths: Amazingly wide variety of techniques enabling their preparation. J Chromatogr A. 2010;1217:902–24. [PubMed: 19828151]
22. Dziomba S, Araya-Farias M, Smadja C, Taverna M, Carbonnier B, Tran NT. Solid supports for extraction and preconcentration of proteins and peptides in microfluidic devices: A review. Anal Chim Acta. 2017;955:1–26. [PubMed: 28088276]
23. Pandey C, Augustine S, Kumar S, Kumar S, Nara S, Srivastave S, Malhotra B. Microfluidics based point-of-care diagnostics. Biotechnol J. 2018;13:1700047.
24. Nge PN, Rogers CI, Woolley AT. Advances in Microfluidic Materials, Functions, Integration, and Applications. Chem Rev. 2013;113:2550–83. [PubMed: 23410114]
25. Erickson D, Li D. Integrated microfluidic devices. Anal Chim Acta. 2004;507:11–26.
26. Hu J, Cui X, Gong Y, Xu X, Gao B, Wen T, Lu TJ, Xu F. Portable microfluidic and smartphone-based devices for monitoring of cardiovascular diseases at the point of care. Biotechnol Adv. 2016;34;305–20. [PubMed: 26898179]
27. Yazdi AA, Popma A, Wong W, Nguyen T, Pan Y, Xu J. 3D printing: an emerging tool for novel microfluidics and lab-on-a-chip applications. Microfluid Nanofluidics. 2016;20:50.
28. Berman B 3-D printing: The new industrial revolution. Bus Horiz. 2012;55:155–62.
29. Stansbury JW, Idacavage MJ. 3D printing with polymers: Challenges among expanding options and opportunities. Dent Mater. 2016;32:54–64. [PubMed: 26494268]
30. Beauchamp MJ, Nordin GP, Woolley AT. Moving from millifluidic to truly microfluidic sub-100-μm cross-section 3D printed devices. Anal Bioanal Chem. 2017;409:4311–19. [PubMed: 28612085]
31. Shallan AI, Smejkal P, Corban M, Guijt RM, Breadmore MC. Cost-Effective Three-Dimensional Printing of Visibly Transparent Microchips within Minutes. Anal Chem. 2014;86:3124–30. [PubMed: 24512498]
32. Anciaux SK, Geiger M, Bowser MT. 3D Printed Micro Free-Flow Electrophoresis Device. Anal Chem. 2016;88:7675–82. [PubMed: 27377354]
33. Anderson KB, Lockwood SY, Martin RS, Spence DM. A 3D printed fluidic device that enables integrated features. Anal Chem. 2013;85:5622–6. [PubMed: 23687961]
34. Sochol RD, Sweet E, Glick CC, Venkatesh S, Avetisyan A, Ekman KG, Raulinaitis A, Tsai A, Wienkers A, Korner K, Hanson K, Long A, Hightower BJ, Slatton G, Burnett DC, Massey TL.,

Iwai K, Lee LP, Pister KSJ, Lin L. 3D printed microfluidic circuitry via multijet based additive manufacturing. Lab Chip. 2016;16:668–78. [PubMed: 26725379]

35. Han HT, Zheng ZX, Pan DW, Wang CC, Hu XP, Wang YC. Portable microfluidic chip electrophoresis device with integrated Pt electrodes for the analysis of AgNPs. Micro Nano Lett. 2018;13:302–5.
36. Sochol RD, Sweet E, Glick CC, Venkatesh S, Avetisyan A, Ekman KG, Raulinaitis A, Tsai A, Wienkers A, Korner K, Hanson K, Long A, Hightower BJ, Slatton G, Burnett DC, Massey TL, Iwai K, Lee LP, Pister KSJ, Lin L. 3D printed microfluidic circuitry via multijet based additive manufacturing. Lab Chip. 2016;16:668–78. [PubMed: 26725379]
37. Lee KG, Park KJ, Seok S, Shin S, Kim DH, Park JY, Heo YS, Lee SJ, Lee TJ. 3D printed modules for integrated microfluidic devices. RSC Adv. 2014;4:32876–80.
38. Lee JM, Zhang M, Yeong WY. Characterization and evaluation of 3D printed microfluidic chip for cell processing. Microfluid Nanofluid. 2016;20:1–15. 22
39. Gong H, Beauchamp M, Perry S, Woolley AT, Nordin GP. Optical approach to resin formulation for 3D printed microfluidics. RSC Adv. 2015;5:106621–32. [PubMed: 26744624]
40. Gong H, Bickham BP, Woolley AT, Nordin GP. Custom 3D printer and resin for 18 μm × 20 μm microfluidic flow channels. Lab Chip. 2017;17:2899–909. [PubMed: 28726927]
41. Beauchamp MJ, Gong H, Woolley AT, Nordin GP. 3D printed microfluidic features using dose control in X, Y, and Z dimensions. Micromachines. 2018;9:326-1–326-12.
42. Sahore V, Kumar S, Rogers CI, Sonker M, Jensen JK, Woolley AT. Pressure-actuated microfluidic devices for electrophoretic separation of pre-term birth biomarkers. Anal Bioanal Chem. 2016;408:599–607. [PubMed: 26537925]
43. Gong H, Woolley AT, Nordin GP. 3D printed high density, reversible, chip-to-chip microfluidic interconnects. Lab Chip. 2018;18:639–47. [PubMed: 29355276]
44. Gong H, Woolley AT, Nordin GP. High density 3D printed microfluidic valves, pumps, and multiplexers. Lab Chip. 2016;16:2450–8. [PubMed: 27242064]

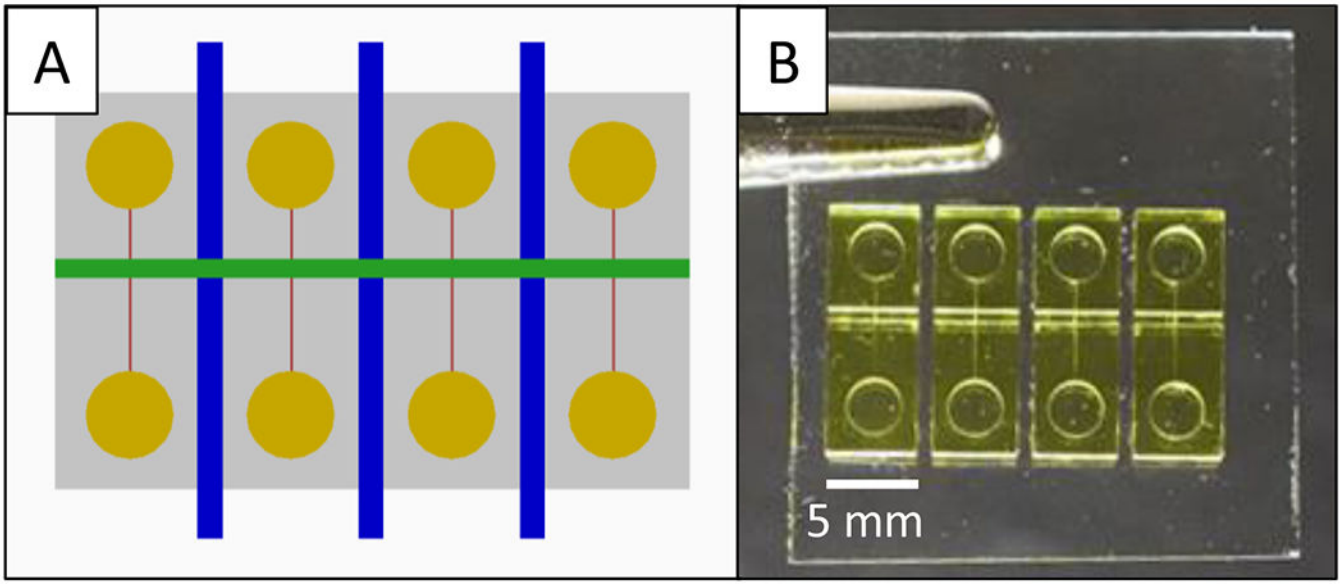

Figure 1.

Devices used for experiments. (A) OpenSCAD design of 3D printed microfluidic device. Reservoirs are yellow, channels are red, the MPW is green, and device divisions are blue. (B) Photograph of 3D printed device.

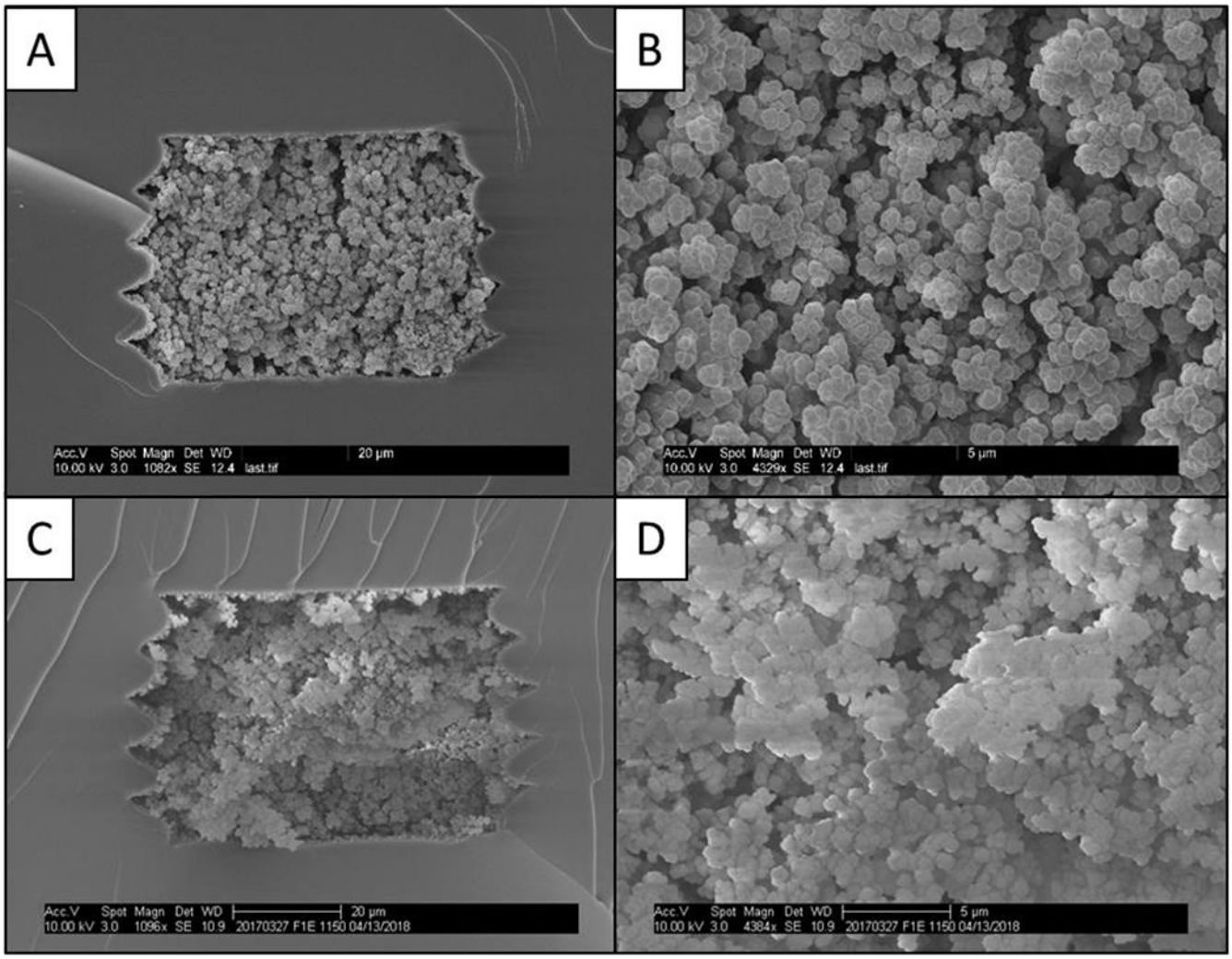

Figure 2.

SEM images of prepared monoliths. (A) Monolith 1. (B) Zoomed view of monolith 1, showing pores and nodules. (C) Monolith 2. (D) Zoomed view of monolith 2, showing pores and nodules.

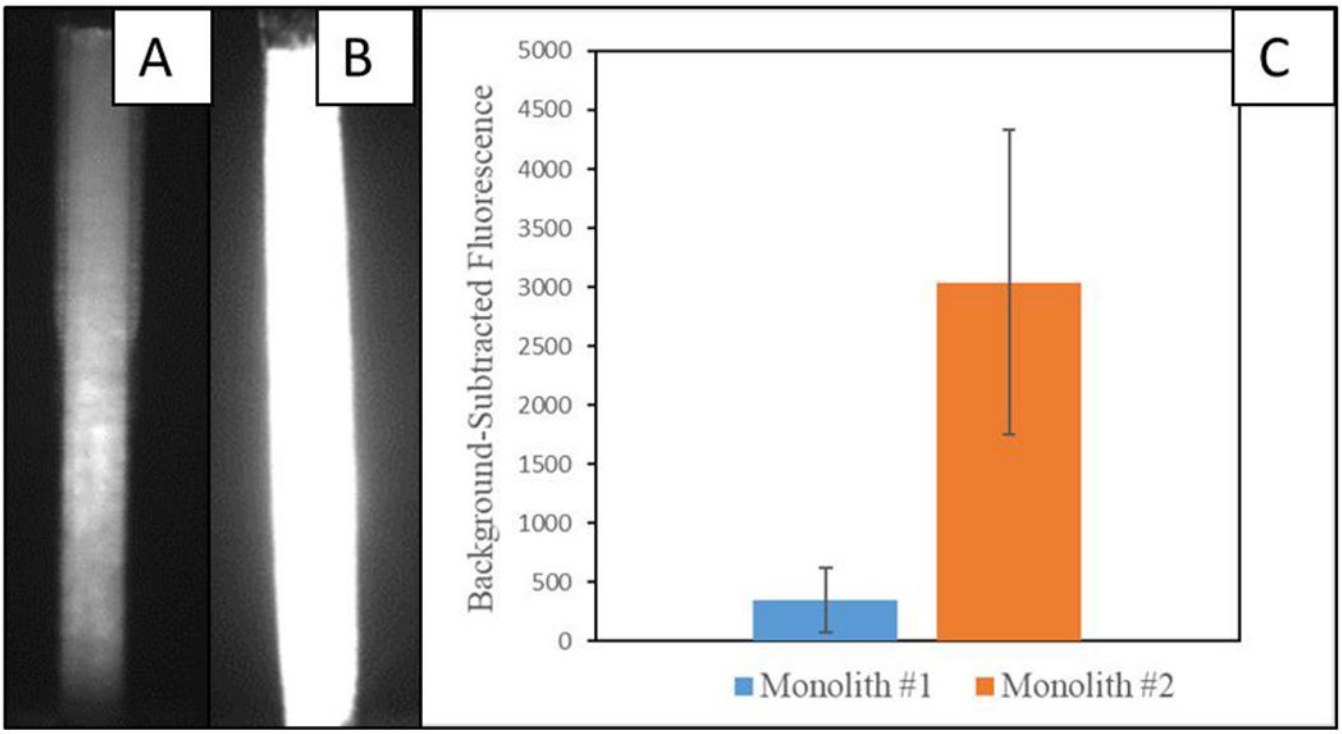

Figure 3.

Labeled antibody attachment. (A) CCD image of monolith 1 with labeled antibody attached. (B) CCD image of monolith 2 with labeled antibody attached. (C) Background-subtracted fluorescence of monolith 1 and monolith 2 after immobilization of labeled antiferritin. Error bars indicate ± 1 standard deviation (n = 3).

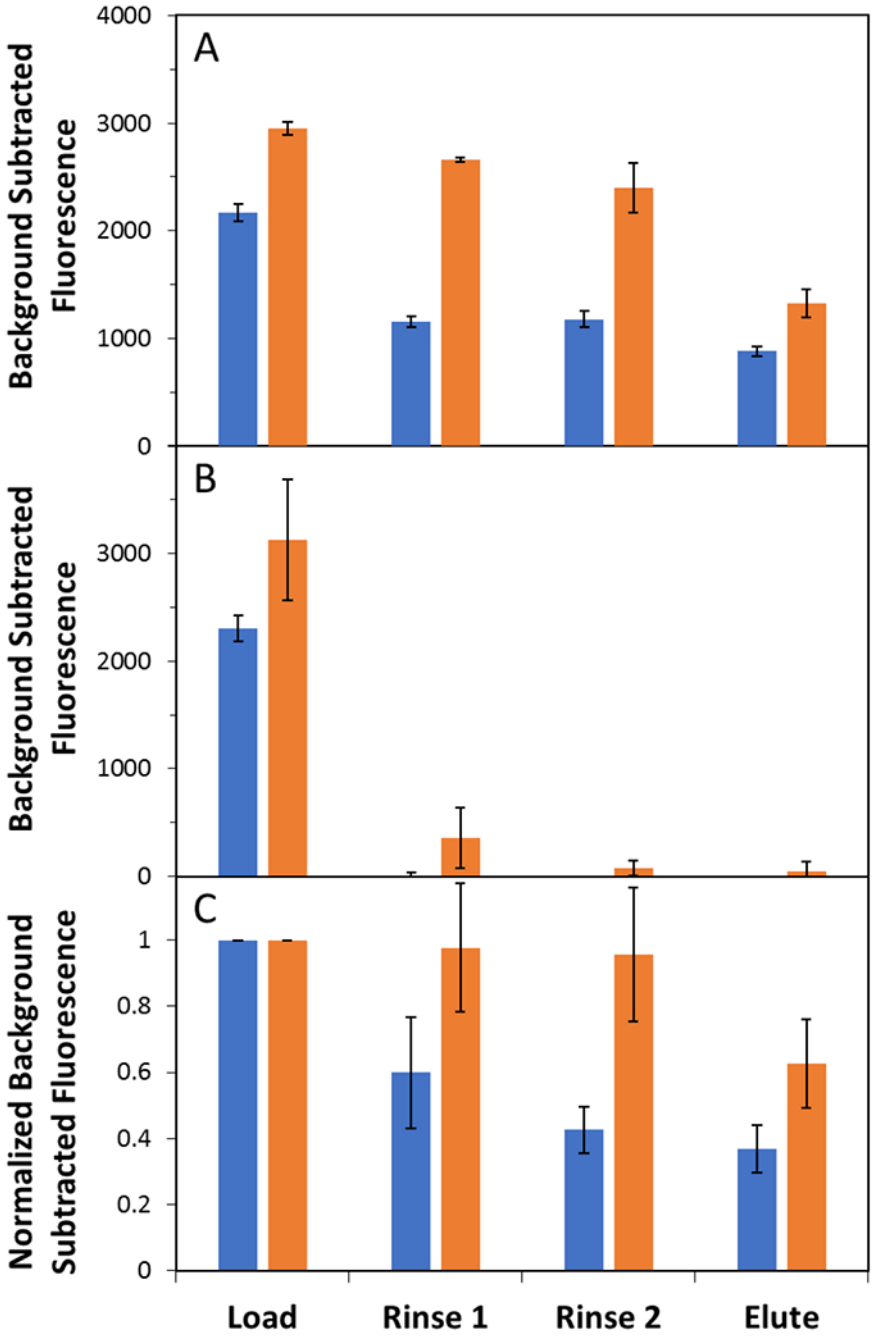

Figure 4:
Immunoaffinity monolith extraction of PTB biomarkers. Control monoliths (no antiferritin) are in blue and monoliths with antiferritin are shown in orange. (A) 50 nM ferritin. (B) 1 μM CRF. (C) Human blood serum (diluted 5-fold) and spiked to 50 nM ferritin.